Chemical redistribution and change in crystal lattice parameters during stress relaxation annealing of the AD730™ superalloy

Malik Durand [a,g,*], Jonathan Cormier [b], Fabien Paumier [c], Shyam Katnagallu [d,e],
Aparna Saksena [d], Paraskevas Kontis [d,i], Florence Pettinari-Sturmel [f], Muriel Hantcherli [f],
Jean-Michel Franchet [g], Christian Dumont [h], Nathalie Bozzolo [a]

[a] *Mines ParisTech, Centre de Mise en Forme des Matériaux (CEMEF), UMR CNRS, PSL University, 1 rue Claude Daunesse, CS 10207, Sophia Antipolis, 06904, France*
[b] *UPR CNRS 3346, Physics and Mechanics of Materials Department, Institut Pprime, ISAE-ENSMA, 1 avenue Clément Ader, BP 40109, Futuroscope-Chasseneuil, 86961, France*
[c] *UPR CNRS 3346, Physics and Mechanics of Materials Department, Institut Pprime, Université de Poitiers, SP2MI, 11 boulevard Marie et Pierre Curie, TSA 41123, Futuroscope-Chasseneuil, 86962, France*
[d] *Max-Planck-Institut Für Eisenforschung, Max-Planck-Strasse 1, Düsseldorf 40237, Germany*
[e] *Institute of Nanotechnology, Karlsruhe Institute of Technology (KIT), Hermann von Helmoltz platz, Eggenstein Leopoldshafen 76344, Germany*
[f] *CEMES, CNRS, INSA, University of Toulouse, 29 rue Jeanne Marvig, BP 94347, Toulouse 31055, France*
[g] *SafranTech-Material and Process Department, Safran SA, rue des jeunes bois, CS 80112, Magny les Hameaux 78114, France*
[h] *Research and Development Transformation Department, Aubert and Duval, Rue du Villa, Les Ancizes 63770, France*
[i] *Department of Materials Science and Engineering, NTNU Norwegian University of Science and Technology, Hogskoleringen 1, Trondheim 7034, Norway*

ABSTRACT

The present study aims to understand the underlying mechanisms of macroscopic contraction that occurs in γ/γ' nickel based superalloys submitted to isothermal annealing and resulting in stress relaxation retardation. Samples of the AD730™ alloy were characterized at different scales using dilatometry, X-Ray Diffraction (XRD) with *in-situ* heating, Electron Channeling Contrast Imaging (ECCI) in the Scanning Electron Microscope (SEM), conventional Transmission Electron Microscopy (TEM) and Atom Probe Tomography (APT). APT analyses revealed chemical composition changes in both the γ matrix and the γ' hardening precipitates during annealing at 760°C after sub-solvus solution heat treatment. These chemical alterations lead to a decrease of the lattice parameters of both phases, which was captured by XRD analyses. The macroscopic volume contraction is shown to be mainly governed by that decrease in the lattice parameters. In addition, from APT analyses, the chemical alterations seem to be promoted by diffusion of solutes such as Cr, Co and Fe, along dislocations occurring under relaxation testing conditions.

1. Introduction

Cast and wrought polycrystalline γ/γ' nickel-based superalloys are used for the manufacturing of aero-engines turbine disks and rings to sustain a combination of high temperatures and high mechanical stresses to which these parts are submitted under engine operating conditions [1,2]. Turbine disks are produced from billets by multistep hot forging sequences followed by heat-treatments to control and optimize the final microstructure. Given the complexity of the thermomechanical routes used for the manufacturing of disks and because of thermal gradients developing during cooling,

high levels of residual stresses exist in the raw forgings [3,4]. Stress relaxation annealing must then be performed after forging which is crucial to ease subsequent machining operations.

It has been previously shown that stress relaxation in the AD730™ alloy is sluggish during the first 20 – 25 h of a stress relaxation test conducted at 760°C starting from a 500 MPa initial stress (i.e. under an applied constant mechanical strain ε of 0.28%) [5]. This slow relaxation regime is associated with an intrinsic tendency for volume contraction as demonstrated by analyzing the material behavior when submitted to an isothermal dilatometric test (Fig. 1).

Other γ/γ' and γ/γ'' nickel superalloys such as Nimonic 80A, Nimonic 101, Nimonic 105 [6], Inconel 718 [7] or Inconel 783 [8] also present such an atypical behavior. The tendency for stress increase retarding relaxation was attributed to a macroscopic isothermal contraction phenomenon [6–8]. Other studies have ev-

M. Durand, J. Cormier, F. Paumier et al.
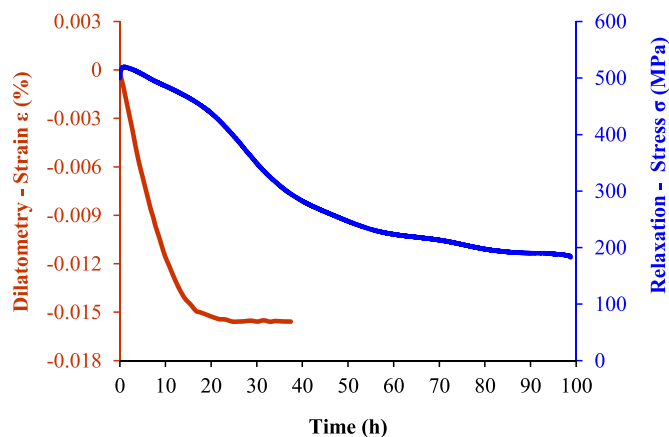
Fig. 1. Behavior of the AD730[TM] alloy submitted to a stress relaxation test at 760°C under 500 MPa initial stress (in blue) and to an isothermal dilatometric test at 760°C (in red) [5].

idenced negative creep (negative strain) for the same reasons in the γ/γ'' Inconel 718 alloy [7] and the γ/γ' IN100 alloy [9]. Understanding the physical origin of the isothermal contraction behavior is thus of utmost practical importance, for the optimization of stress relaxation treatments, for the control of in-service mechanical behavior, and for the dimensional control of components. This is a challenging fundamental issue due to the different scenarios that could potentially rationalize this behavior. The most probable hypothesis proposed to explain the behavior of the AD730[TM] alloy is based on changes in the chemical composition of the γ' precipitates and of the γ matrix. This assumption is further investigated in the present article. Few reports discuss the evolution of compositions during aging of γ/γ' or γ/γ'' superalloys [7,10–12]. Chemical changes are assessed either indirectly through the evolution of γ, γ' or γ'' lattice parameters studied by X-Ray Diffraction (XRD) or Neutron Diffraction (ND) or directly by using Atom Probe Tomography (APT). These reports show that the decrease in the γ, γ' or γ'' lattice parameter can be related to the precipitation of γ'' and γ' phases [7] or to the redistribution of chemical elements (Ni, Cr, Ti, Al and Co) between the γ matrix and the coherent γ' hardening precipitates [10,11].

In this work, specimens of the AD730[TM] alloy after relaxation test at 760°C / 500 MPa / 40 h or isothermal holding at 760°C / 40 h were submitted to investigations by X-Ray Diffraction (XRD), Electron Channeling Contrast Imaging (ECCI) in the Scanning Electron Microscope (SEM), conventional Transmission Electron Microscopy (TEM) and Atom Probe Tomography (APT), combined to seek for local chemical changes and their effect on lattice parameters. The first part of this study (Section 3.1) presents the influence of temperature on the composition of γ and γ' phases and the evolution of their lattice parameters. The second part (Section 3.2) deals with the role played by dislocations in composition evolutions. The discussion of the results at different microstructural scales and down to the near-atomic level, allows a better understanding of the mechanisms and their consequence on the macroscopic behavior of the material.

2. Material, experimental approach and procedures

2.1. Material and dilatometry tests

The AD730[TM] alloy is a new cast and wrought γ/γ' superalloy developed for turbine disk application by the Aubert & Duval company [13,14], with the chemical composition given in Table 1.

Like any γ/γ' nickel-based superalloy, the AD730[TM] alloy has γ'-Ni$_3$(Al, Ti) precipitates with L1$_2$ ordered cubic structure and

different sizes, morphologies and chemical compositions [15–17], depending on the cooling rate experienced at the time (and thus temperature) of their formation. These precipitates are strengthening the polycrystalline Face Centered Cubic (FCC) disordered solid solution, referred to as γ-matrix, and pin the grain boundaries. Both polycrystalline and single crystal versions of the AD730[TM] alloy have been used in this work. With the same chemical composition, these materials were used to decouple the effects of grain boundaries and intragranular hardening precipitation. For collecting Scanning Electron Microscopy (SEM) micrographs, the samples were first mechanically mirror polished and then the γ matrix was slightly dissolved by electrochemical etching, with an electrolyte made of 45% sulfuric acid, 42% nitric acid and 13% phosphoric acid, at 0-5°C for 2 s under 1 V [5].

Polycrystalline (PX) samples were all machined out from the same industrial AD730[TM] forging provided by Safran. The as-received material has a fine-grained microstructure (about 10 μm) optimized to provide the best compromise between static and cyclic (fatigue) properties [18]. Rods of the as-received material (14 mm in diameter) were cut and submitted to a γ'-subsolvus solution treatment: 1080°C $\pm$ 5°C for 4 h followed by cooling at 100°C/min. The solvus temperature (T$_{solvus}$) of the γ' phase is about 1105°C [17,19]. The subsolvus solution treatment allows to keep the largest (so-called primary) precipitates undissolved to pin the matrix grain boundaries and preserve the fine grain size [20]. The size and distribution of secondary and tertiary precipitates (which form during cooling after holding at the subsolvus solution treatment temperature) and the partitioning of elements between the γ matrix and the different types of γ' precipitates are controlled by the cooling rate [20,21]. After the 4 h holding at 1080°C, the PX samples have a 5% area fraction of primary γ' precipitates (called γ'(I) in the following) with an equivalent circle diameter of 1-5 μm and which are mainly located at the grain boundaries (Fig. 2a) [18,22,23]. Secondary γ' precipitates (called γ'(II) in the following) are about 95 nm in size, intragranular and coherent with the matrix (Fig. 2b). Tertiary γ' precipitates (γ'(III)) found between secondary ones are much finer and also coherent with the matrix. Furthermore, owing to the small size of the rods and their slow cooling, it can be assumed that the samples are free of residual stress after the sub-solvus solution treatment. In the following, "PX initial state" refers to that state obtained after sub-solvus solution treatment and controlled cooling.

The single crystalline (SX) bars, also provided by Safran bars are all coming from the same batch (i.e. same ingot, same melt and same solidification parameters). Specimens were machined from bars whose solidification direction was close to a <001> crystallographic direction. The size of SX bars is close to that of the machined polycrystalline rods. The as-received cast samples were first homogenized for 24 h at 1180°C and then for 24 h at 1200°C followed by air cooling. The γ' precipitation was adjusted to be similar to that of the PX initial state by performing another heat treatment: holding for 2 h at 1120°C (i.e. above the solvus temperature) followed by slow cooling ($\sim$ 80°C/min). The resulting size distribution of γ'(II) precipitates (Fig. 2d) is very similar to that of the polycrystalline material (Fig. 2c). The area fraction of secondary precipitates f_S is 43% in the SX material, higher compared to the PX material (33%) because of the absence of primary precipitates in the SX material. This state obtained after thermal treatments will be referred to as the "initial state" of the SX material in the following.
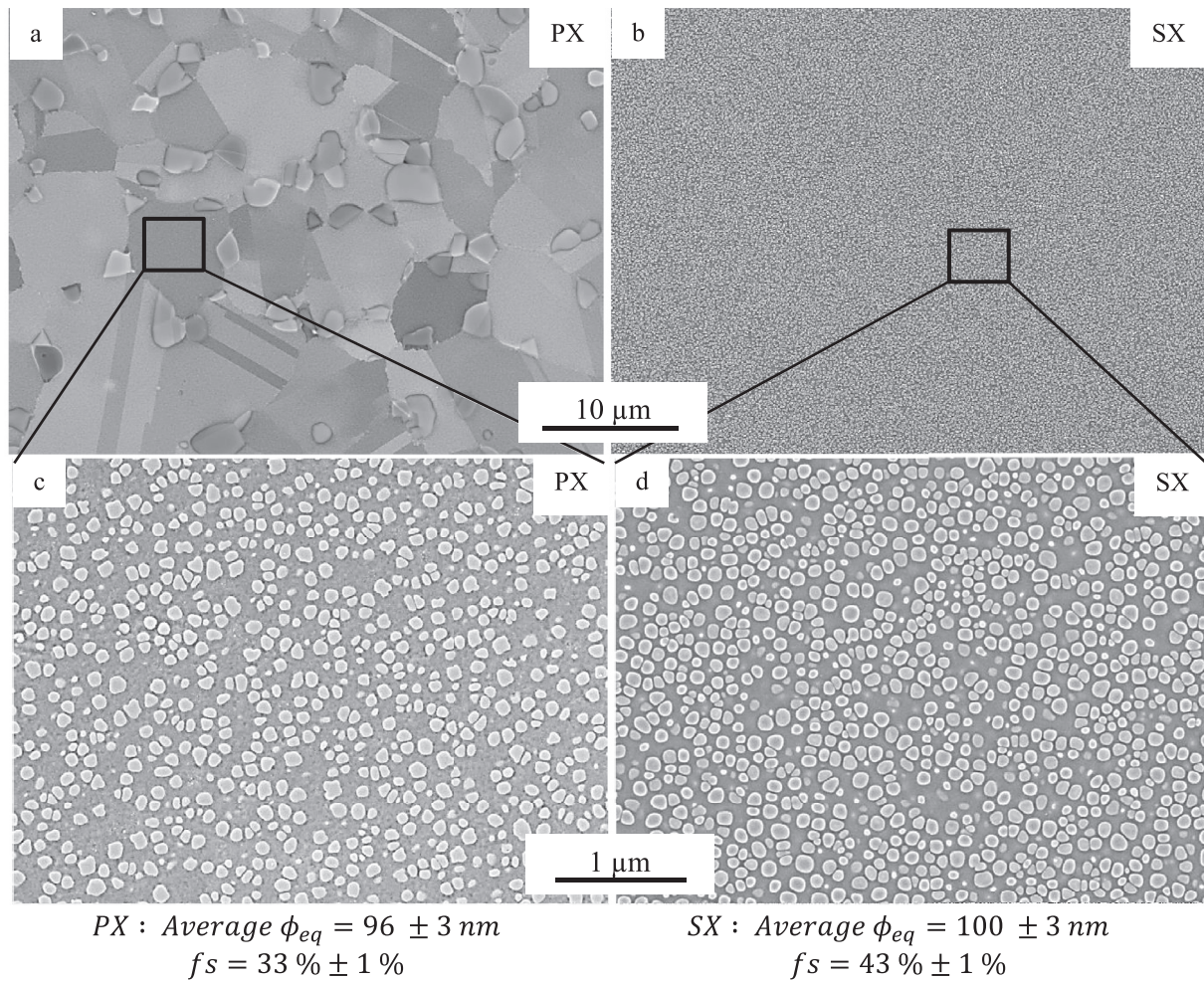
Isothermal dilatometry has been performed at 760°C on both the PX and the SX alloys, aiming to measure their macroscopic contraction magnitude. The PX material was also subjected to a relaxation test at 760°C for 40 h starting from 500 MPa initial stress. The specimen gauge length and the grip section of the same relaxation test piece were analyzed. The later on called "relaxation

Table 1
AD730™ chemical composition (weight and atomic %).

Element	Ni	Cr	Co	Fe	Ti	Mo	W	Al	Nb	C	B
Wt. %	Bal	16.0	8.5	4.0	3.5	3.0	2.6	2.3	1.1	0.01	0.01
At. %	Bal	17.4	8.2	4.2	4.1	1.7	0.8	4.8	0.7	0.07	0.05

Table 2
Summary of the characterization techniques and analyzed samples.

		APT	TEM	ECCI	XRD *in situ* 760°C	Dilatometry 760°C
	Initial state	✓	✓	✓		✓
PX	Relaxation grip 760°C / 40 h	✓		✓		
	Relaxation gauge 500 MPa 760°C / 40 h	✓	✓	✓		
SX	Initial state				✓	✓

$$PX : Average\ \phi_{eq} = 96 \pm 3\ nm$$
$$fs = 33\ \% \pm 1\ \%$$

$$SX : Average\ \phi_{eq} = 100 \pm 3\ nm$$
$$fs = 43\ \% \pm 1\ \%$$

Fig. 2. (a) Low magnification SEM BackScattered Electron (BSE) image showing γ'(I) precipitates and grain size in the PX initial state and (b) SEM Secondary Electron (SE) image of the SX initial state at the same magnification as (a). (c, d) SEM SE images of the γ'(II) precipitates in the (c) PX and (d) SX initial microstructures, and their quantification in terms of average equivalent circle diameter and area fraction.

grip" microstructure is that of the specimen taken in the grip section: it was subjected to temperature but not to deformation, whereas the specimen gauge length was subjected to both temperature and deformation ("relaxation gauge" microstructure). Both microstructures, as well as the initial one have been analyzed by APT, in order to decouple the influence of temperature and of applied strain/stress on the local composition changes that are suspected to occur at the intragranular scale. Dislocation landscapes have been observed by Transmission Electron Microscopy (TEM). SX samples have been used to seek for changes in the lattice pa-

rameters and misfit by X-Rays Diffraction (XRD). All analyzed samples and techniques used are summarized in Table 2.

During the relaxation test, the sample is heated to the desired temperature and then an external tensile stress is applied up to the desired initial stress. From there, the total strain is kept constant and the stress is followed over time. During the dilatometry tests, the evolution of the dimension along the longitudinal axis is followed as a function of time at constant temperature. The reader is referred to a previous article from the authors for more details on the performed dilatometric and relaxation tests [5].

2.2. Atom probe tomography (APT)

APT specimens were prepared from site specific lift-outs from intragranular regions of PX AD730™ samples using an FEI plasma focused ion beam (PFIB) instrument, following the procedures described in [24] and adapted for PFIB as outlined in [25]. Targeted specimen preparation was conducted by depositing Pt [25]. APT was performed on a local electrode atom probe (LEAP-5000XR) instrument. The specimens were analyzed in laser mode with 50 pJ energy at a pulse repetition rate of 125 kHz and at 50 K. APT analysis was performed using the proprietary IVAS 3.8.8 software.

2.3. X-ray diffraction (XRD)

Crystal lattice parameter changes as a function of temperature and time were tracked by XRD using a Bruker D8 diffractometer equipped with a copper X-ray source (operated under 40 kV and 40 mA) and with a high-temperature chamber (as described in chapter 4 of Ref. [26]). Experiments were performed under high vacuum ($< 10^{-6}$ mbar) to limit oxidation of the specimens' surfaces.

The detector used is the Lynxeye™, it is a linear detector discriminating in energy and is composed of 192 spot detectors which provides a very good signal to noise ratio. The diffractometer is also equipped with a high-temperature heating chamber allowing *in-situ* monitoring of the evolution of the lattice parameter as a function of temperature and time. The furnace is of the Anton Paar company, it is covered with a graphite dome transparent to X-rays and which allows a homogeneous temperature. The heating rate is $1°C.s^{-1}$.

The expansion of the furnace was first calibrated. The intrinsic dilatation of the furnace was measured to be less than $1.10^{-7}°C^{-1}$ and therefore negligible compared to the variation of the samples. Furthermore, the measurement accuracy of 2θ is guaranteed to be within $0.01°$ ($\Delta 2\theta$) using various reference powders over the entire angular range. The absolute error Δa can then be calculated, and the results are presented in Table 3 for a lattice parameter at room temperature of 3.5910 Å and for different diffraction angles.

SX samples (mechanically polished down to 1 micron with diamond abrasive powder) were used in XRD measurements in order to get higher intensity peaks with a narrower width compared to PX materials, thus enabling the detection of subtle changes. The analyzed (400) diffraction peak has been chosen for its relatively high Bragg angle allowing for better accuracy. The heat treatment consists of a temperature rise at 1°C/s from room temperature up to 760°C, followed by holding at 760°C for 40 h and then a return to room temperature at 1°C/s.

Peak analyses were performed using the "Rayflex-Analyze" and Excel softwares. The fitting of the experimental curves at room temperature was performed by associating to each component a pseudo-Voigt type function, which is a linear combination of a Lorentzian and a Gaussian weighted by a proportionality coefficient η ($0 < \eta < 1$). These normalized functions, characterized by their FWHM (Full Width at Half Maximum) and 2θ position, are commonly used in X-ray diffraction to describe the profile of Bragg peaks. Two tests were carried out at 760°C to check for repro-

Table 3
Calculation of the absolute error on the lattice parameter for different diffraction planes diffraction planes (200), (300) and (400) at room temperature.

Plans (hkl)	2θ (°)	Δa (Å)
200	50	7.10^{-4}
300	80	4.10^{-4}
400	118	2.10^{-4}

ducibility. Diffractogram acquisitions take 200 s for each and have been recorded during the holding of 40 h at 760°C every 10 min. For the readability of the graphs, we have represented only a few of the 300 recorded diffractograms.

2.4. Transmission electron microscopy (TEM)

Conventional TEM observations have been done using a JEOL JEM 2010 transmission electron microscope operated at 200 kV. TEM thin foils have been extracted from slices cut perpendicularly to the tensile axis and prepared by mechanical polishing and further electropolishing in a solution made of 5% perchloric acid and 95% methanol under 60 V at approximately - 30°C.

2.5. Electron channeling contrast imaging (ECCI)

ECCI has been performed using a BSE detector in a Zeiss Supra 40 Field Emission Gun Scanning Electron Microscope (FEG-SEM) operated at 30 kV acceleration voltages and a working distance of 12 mm, on electrolytically polished samples. The electrolyte was then composed of 10% perchloric acid and 90% methanol, and polishing was performed at 5–10°C during 8 s under a voltage of 35 V.

3. Results

The influence of temperature on local compositions will be discussed first, in Section 3.1, by comparing the initial state and the heat-treated state (i.e. relaxation grip sample). The influence of dislocations on γ and γ' composition will be discussed in Section 3.2 by comparing the relaxation grip sample and the relaxation gage sample.

3.1. Evolution during heat treatment

3.1.1. Evolution in local chemical compositions assessed by APT

Fig. 3 shows APT reconstructions of samples taken from intragranular locations of the PX material, in its initial state, after 40 h exposure at 760°C (relaxation grip sample) and after 40 h relaxation test at 760°C from an initial stress of 500 MPa (relaxation gage sample which will be discussed in Section 3.2). Reconstructions contain γ'(II) and γ'(III) precipitates and their interfaces with the γ matrix. The most obvious difference between these three states regards tertiary precipitate size. From these APT reconstructions, the chemical composition of each type of precipitate and the matrix was extracted. For each state, two APT datasets are measured while the compositions given below are the average of the precipitates found in all the measured specimens of each state.

Fig. 4 shows a comparison the compositions of the matrix, of the γ'(II) and of the γ'(III) precipitates in the PX initial state and after heat treatment at 760°C (grip microstructure). The Ni concentration increases in the γ' phase after heat treatment at 760°C (from 65.9 to 69.8 at.% in γ'(II)) and decreases in the γ matrix (from 47.2 to 45.4 at.%). Conversely, Cr and Co concentrations decrease in γ' phase (from 1.5 to 1.1 at.% and from 4.4 to 2.7 at.%, respectively, in γ'(II)) and increase in the matrix (from 23.8 to 26.0 at.% and 11.2 to 12.4 at.%, respectively). A slight decrease in Ti and Al contents is observed in the matrix (from 2.2 to 1.5 at.% and from 2.9 to 2.0 at.% respectively), compensated by an increase in the tertiary precipitates (from 7.0 to 7.8 at.% and from 9.3 to 10.6 at.% respectively).

Compositional variations in the γ matrix due to the presence of tertiary γ' precipitates have also been investigated. In a previous study in a powder metallurgy superalloy, it was shown that the composition of the γ matrix was affected by the presence of
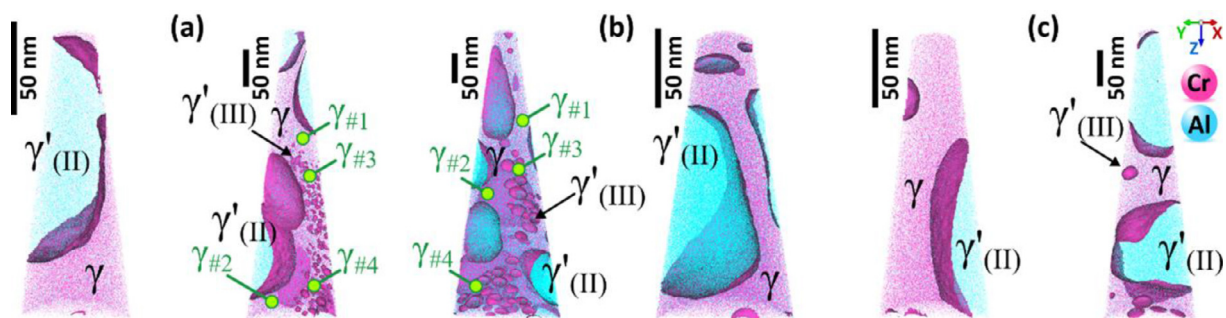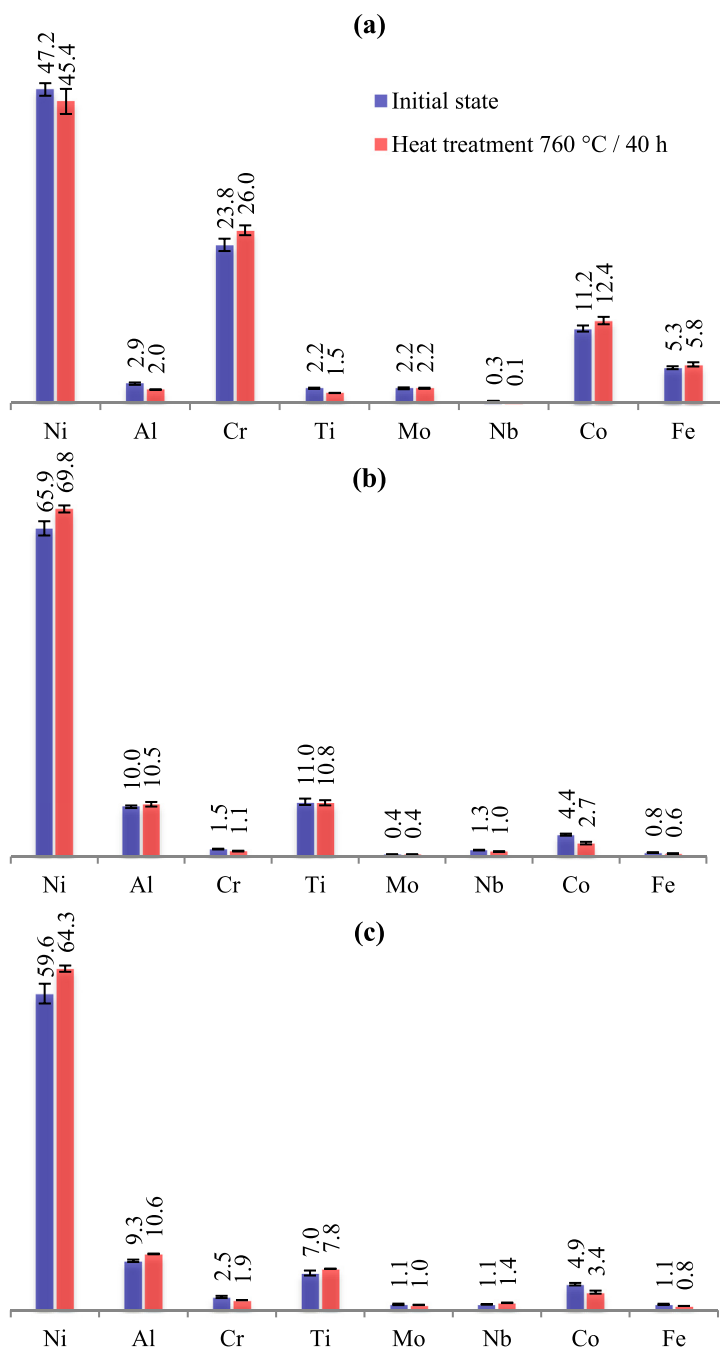
Fig. 3. APT reconstructions of specimens taken from intragranular locations of PX samples: (a) initial state, (b) relaxation grip sample after 40 h at 760°C and (c) relaxation gauge sample after 40 h at 760°C starting from 500 MPa. The γ/γ' interfaces are shown with an iso-composition surface at 13 at. % Cr.

Fig. 4. Chemical composition (at.%) of (a) the matrix, (b) secondary and (c) tertiary γ' precipitates before (blue bars) and after (red bars) holding for 40 h at 760°C. The numbers on top of each bar are the atomic fraction values obtained from APT datasets (i.e. exact bar height).

Table 4
Summary of γ matrix composition from locations as denoted in Fig. 3a and b, for the initial state and after heat treatment at 760°C (at.%).

		Ni	Al	Cr	Ti	Mo	Nb	Co	Fe
					Initial state				
close to γ/γ'	$\gamma_{\#1}$	47.3	2.9	24.8	2.1	2.2	0.3	11.1	5.4
	$\gamma_{\#2}$	47.2	3.2	24.5	2.1	2.4	0.3	12.0	5.5
close to γ'(III)	$\gamma_{\#3}$	47.4	2.9	23.1	2.3	2.2	0.4	10.9	5.1
	$\gamma_{\#4}$	45.7	2.7	22.6	2.0	2.0	0.3	11.3	5.0
				Grip sample after heat treatment at 40 h at 760°C					
close to γ/γ'	$\gamma_{\#1}$	46.1	1.9	26.6	1.5	2.5	0.1	12.1	5.9
	$\gamma_{\#2}$	46.0	1.9	25.9	1.5	2.4	0.1	12.3	5.8
close to γ'(III)	$\gamma_{\#3}$	41.8	1.9	24.9	1.5	2.3	0.1	13.4	5.3
	$\gamma_{\#4}$	44.8	2.0	25.5	1.5	2.5	0.2	12.5	5.7
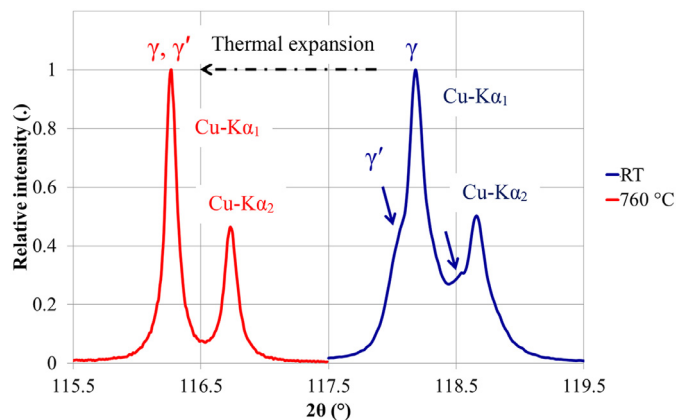
Fig. 5. (400) XRD peak of the SX alloy at room temperature and at 760°C just after heating (heating rate: 1°C.s⁻¹ / Stabilization at 760°C for 30 min / 2θ scan time: 200 s).

the tertiary γ' precipitates [27]. With this in mind, we have investigated the γ matrix composition close to the γ/γ' interface and close to tertiary γ' precipitates corresponding to locations indicated in Fig. 3a and b. Table 4 shows the composition measured by APT for all these locations. At the initial state, no variation is observed between the two different locations. Only in the case of Cr, there is an indication of higher amounts of Cr close to the γ/γ' interface. Although no variations observed also after heat treatment at 760°C (grip microstructure), there are some indications that Ni content is higher closer to γ/γ' interface. However, substantial variations and a clear compositional trend is not observed as in the previous study of the powder metallurgy superalloy [27].

3.1.2. Lattice parameter and misfit evolution assessed by XRD
3.1.2.1. During heating from room temperature to 760°C
Fig. 5 shows the (400) Cu-Kα_1 and -Kα_2 XRD peaks of the SX alloy at room temperature (RT, plotted blue) and at 760°C after heating at 1°C.s⁻¹ (plotted red).

The (400) peak contains overlapping contributions from both the matrix γ and the γ' precipitates. The γ' and γ phases give superimposed peaks due to their close values of lattice parameters. The peaks exhibit a secondary peak or shoulder (blue arrows) at RT which disappears at 760°C, suggesting a very small difference in lattice parameter between both phases at room temperature which vanishes upon heating. The peaks clearly shift to lower diffraction angles at higher temperatures, by roughly 2°, as a result of thermal expansion and increase in lattice parameters. The main and secondary peaks have been attributed to γ and γ' phases as follows. Many studies have shown that the thermal expansion of the γ' phase is less than that of the matrix in other γ/γ' nickel-based superalloys [28–36]. The peak of the γ' phase therefore shifts to a lesser extent than the peak of the γ matrix when the temperature

increases. It can thus be deduced that the γ' phase is responsible for the left peak shoulder while the high narrow peak on the right is that of the matrix.

The constrained lattice misfit (defined below) is then positive at room temperature and tends towards zero when increasing temperature.

The lattice parameter misfit noted δ is defined as follows (Eq. (1)):

$$\delta = 2 \times \frac{a_{\gamma'} - a_\gamma}{a_{\gamma'} + a_\gamma} \tag{1}$$

where a_γ is the lattice parameter of γ matrix and $a_{\gamma'}$ is the lattice parameter of γ' phase.

The lattice parameter depends on the chemical composition of the alloy. Moreover, the coherency of γ'(II) and γ'(III) precipitates with the matrix leads to elastic deformation of both the γ and γ' phases and accommodated lattice parameters at the interface. A constrained lattice parameter should then be considered [37], which depends on the microstructure, and notably on the precipitate size, composition, volume fraction and degree of coherency that are themselves dependent on the thermal history of the material.

It is worth noticing that, in principle, XRD analyses can be used to trace back to the constrained misfit. However, this measurement is a weighted average depending on precipitate size and γ channel width. In order to obtain the constrained lattice parameter misfit, it is necessary to work on a model material such as the SX alloy used in the present work. Only then, it is possible to perform finite element calculations to obtain the associated stress in the matrix and the precipitates [38].
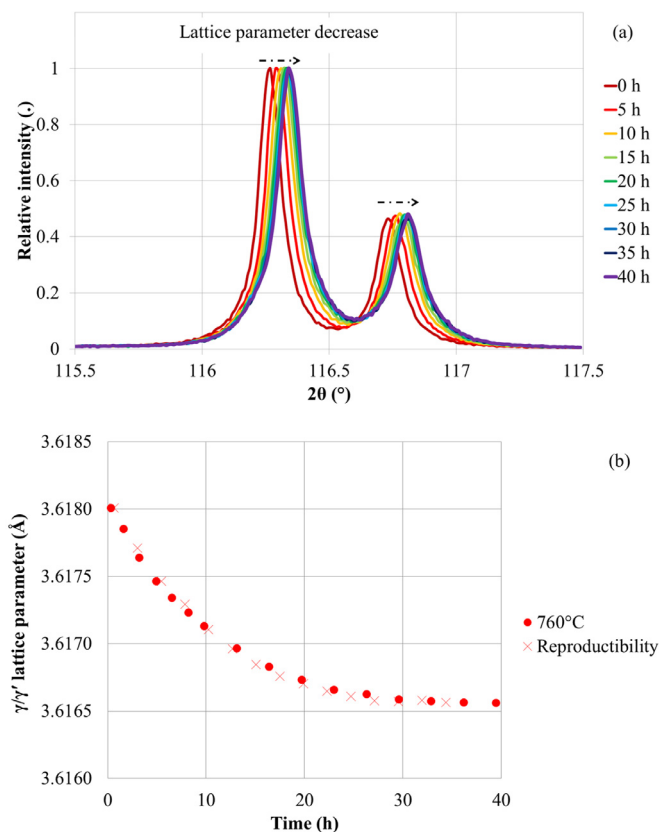
3.1.2.2. During holding at 760°C
The (400) XRD peak was monitored during 40 h holding at 760°C, as shown in Fig. 6. Gradual peak shift towards higher 2θ values was observed (Fig. 6a). This shift necessarily reflects a decrease of the lattice spacing d_{hkl} and thus of the lattice parameter.

The evolution of the lattice parameter value evaluated using the Kα_1 (400) diffraction peak is shown on Fig. 6b. The same results were obtained using the Kα_2 diffraction peaks (not shown here) and the experiment showed excellent reproducibility (data from a second run plotted with cross symbols on Fig. 6b). The lattice parameter gradually decreases during about 25 h before stabilizing (Fig. 6b). No shoulder re-appearance can be seen on either side of the peaks; which suggests that both the γ- and the γ'-phase lattice parameters keep being very close to each other.

3.1.2.3. After cooling back to room temperature
Fig. 7 compares the XRD diffractograms obtained at room temperature before and after the heat treatment (40 h at 760°C). They do not overlap, which shows that the material has evolved at high temperature and does not recover its initial state, in other words it has undergone a transformation.

Fig. 6. (a) (400) XRD peak evolution of the SX alloy during holding at 760°C for 40 h. (b) γ/γ' lattice parameter evolution deduced from the Cu-Kα_1 diffraction peak positions. Reproducibility was checked by doing the same experiment again (red crosses), and the same results were also obtained from the Cu-Kα_2 diffraction peak (but not shown here).
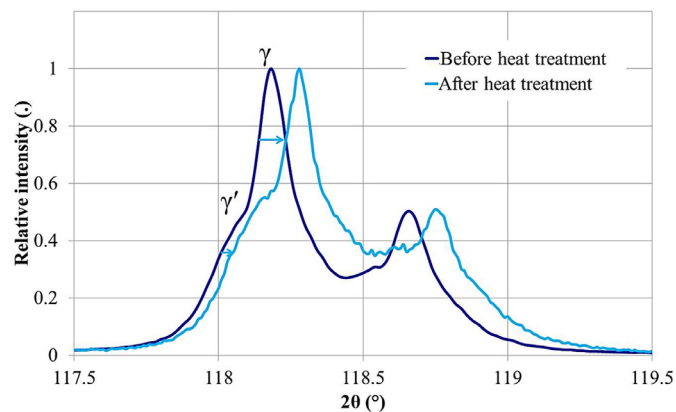

Fig. 7. (400) XRD peak of the SX alloy at room temperature before and after heat treatment at 760°C for 40 h.

To measure precisely the peak shift due to the transformation that occurred during heat treatment, peak deconvolution was performed. Moreover, the peaks (300) were measured in addition to the (400) peaks after heat treatment (Fig. 8). Since the Miller indices h, k, and l are of different parity for the (300) peak, there is an extinction condition for the FCC γ matrix. That is, unlike peak (400) where there is the contribution of both the γ phase and the γ' phase, peak (300) includes only the γ' phase.

Thus, thanks to the (300) peak, it is possible to get the lattice parameter of the γ' phase: 3,5931 Å. From this data the position of the γ' peak can be set on the (400) diffractogram. With this
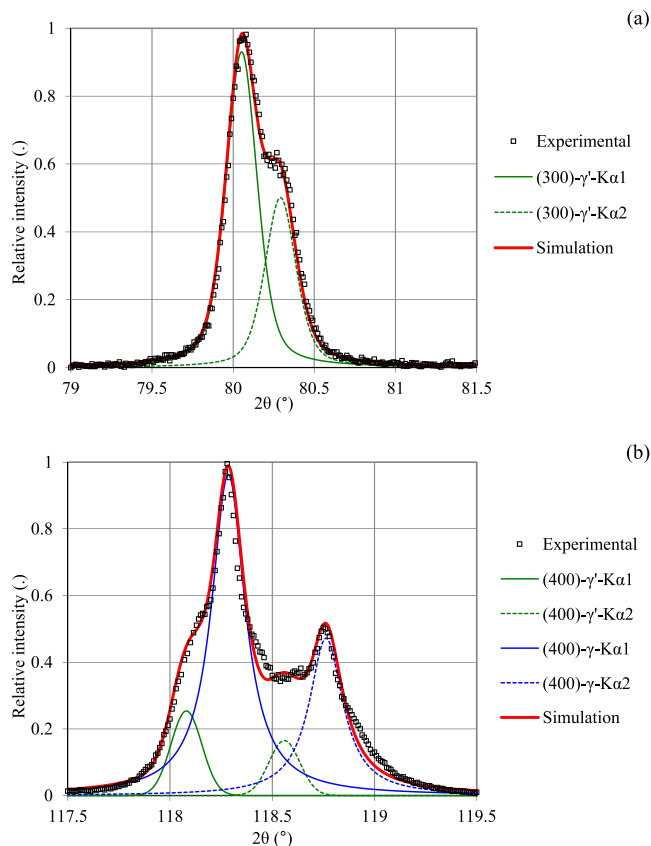
Fig. 8. Diffractograms of AD730^{TM} alloy SX-100 measured at RT after the thermal treatment (40 h at 760°C) (a) γ'-(300) (b) γ/γ'-(400) peaks.
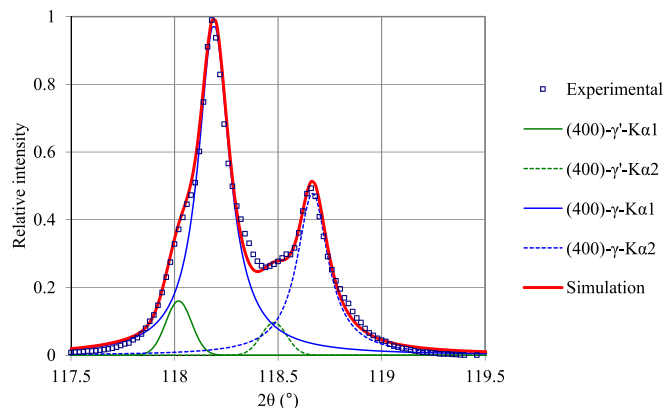
Fig. 9. (400) diffraction peak of the AD730TM alloy SX-100 at room temperature before heat treatment with γ and γ' contributions deconvoluted.

$a_{\gamma'}$ value, the (400)-CuKα_1 peak of the γ' phase should be located at a 2θ value of 118.08 °, which indeed corresponds to the peak shoulder observed on the left side of the (400) peak diffractogram (Fig. 8).

The positions of the γ and γ' peaks after heat treatment (Fig. 8b) can be compared to those before heat treatment (Fig. 9).

The offset in the γ peak position seems to be larger than that of γ' phase: 0.1 ° for γ and 0.05 ° for γ' (Table 5). This suggests that the lattice parameter of the matrix decreased more than that of the precipitates, and that the misfit value after thermal treatment is thus higher than the initial one. The associated contraction deformation of the γ matrix and γ' phase is 0.053% and 0.028%, respectively. With a classical rule of mixture and consider-

Table 5
Positions of the peaks before and after heat treatment and associated deformation.

	Before HT		After HT		Relative difference (%)	Deformation estimated with Eq. (2) (%)
	2θ (°)	a (Å)	2θ (°)	a (Å)		
γ' precipites	118.03	3.5941	118.08	3.5931	-0.028	-0.042
γ matrix	118.19	3.5911	118.29	3.5892	-0.053	
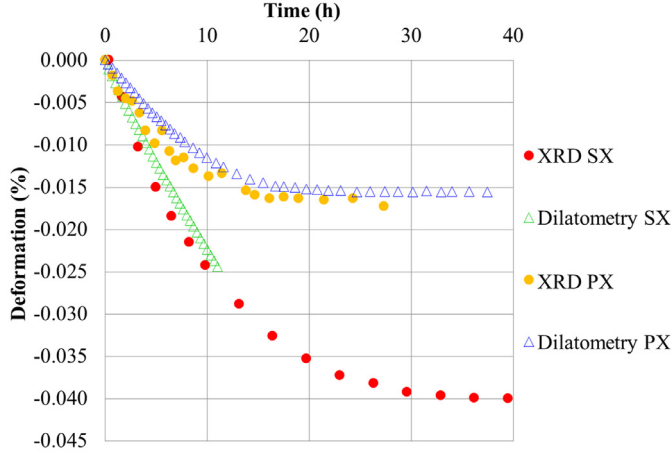
Fig. 10. Contraction strains during holding at 760°C, deduced from (400) XRD peak positions and from isothermal dilatometry.

ing the contribution of the widely prevalent secondary precipitates only (Eq. (2)), the overall deformation is estimated to be of about 0.042%.

$$\bar{\varepsilon}_{DRX} = f_s^{\gamma} \cdot \varepsilon_{DRX}^{\gamma} + f_s^{\gamma'} \cdot \varepsilon_{DRX}^{\gamma'} \tag{2}$$

3.1.3. Relationship between volume shrinkage, chemical composition change and crystal lattice contraction during isothermal holding

Fig. 10 presents the elastic contraction strains deduced from XRD measurement using (Eq. (3)) and from isothermal dilatometry (Eq. (4)) as a function of holding time at 760°C, for the SX alloy. The dilatometry and XRD data obtained from the PX alloy are also shown at this plot and will be commented in Section 4.2. The XRD measured strains were derived here from the overlapped γ matrix and γ' diffraction (400) peak. The dilatometer measured the overall variation of the sample length.

$$\varepsilon_{DRX} = \frac{a_{DRX} - a_{DRX}^0}{a_{DRX}^0} \tag{3}$$

$$\varepsilon_{dilatometry} = \frac{l - l_0}{l_0} \tag{4}$$

XRD results showed a contraction of 0.040% over about 25 h in the SX material. This contraction of the "global" lattice parameter (i.e. including both γ and γ' phases) is in very good agreement with the macroscopic contraction measured by dilatometry, suggesting that the volume contraction is mainly governed by the changes in the lattice parameter of γ' and γ phases.

Changes in lattice parameter were also estimated using the Vegard relationship [39] (Eq. (6)) and the chemical composition changes measured by APT in the PX microstructure submitted to thermal exposure (relaxation grip sample compared to the initial state).

$$a_{Vg}^{\varphi} = a_0^{\varphi} + \Sigma_i \Gamma_i^{\varphi} x_i^{\varphi} \tag{6}$$

where:

- a_{Vg}^{φ} is the lattice parameter of the φ phase (γ or γ'), Γ_i^{φ} are the Vegard coefficients and x_i^{φ} are the molar fractions of each alloying elements i. The Vegard coefficient values found in literature [11,39] are summarized in Table 6.
- a_0^{φ} is the lattice parameters for pure Ni and Ni$_3$Al, $a_{Ni} = 3.524$ Å and $a_{Ni_3Al} = 3.570$ Å [39].

The values of the Vegard coefficients for all considered alloying elements show that an increase in concentration of any of them in the matrix would lead to an increase in lattice parameter. This would be more pronounced in the case of Nb, Mo and Ti, followed by Al, Fe and Cr. An increase in Nb, Mo or Ti contents also increases the lattice parameter of the γ' phase. However, an increase in Co, Cr and Fe content has the opposite effect of decreasing the γ' lattice parameter.

A strain value associated with the variation of the lattice parameters estimated with the Vegard relationship can then be determined by Eq. (5):

$$\varepsilon_{APT} = \frac{a_{Vg}^{\gamma/\gamma'} - a_0^{\gamma/\gamma'}}{a_0^{\gamma/\gamma'}} \tag{5}$$

Where

$$a_{Vg}^{\gamma/\gamma'} = a_{Vg}^{\gamma} \cdot f_s^{\gamma} + a_{Vg}^{\gamma'} \cdot f_s^{\gamma'} \tag{6}$$

Only γ'(II) precipitates have been used for this calculation because their volume fraction is much larger than that of primary and tertiary precipitates. Moreover, taking into account only the secondary γ'(II) precipitates allows to have the deformation in the grain. The results are presented in Table 7.

Using a mixture law Eqs. (5) and ((6)) considering the volume fractions and lattice parameters of the matrix and γ'(II) precipitates results in a contraction of about 0.017% during the heat treatment, a value very close to that obtained by isothermal dilatometry, equal to 0.016% (Fig. 10).

3.2. The role of dislocations on facilitating compositional alterations

It is well known that solutes can segregate at crystal defects, such as dislocations and stacking faults. Recent TEM and APT studies on superalloys have revealed segregation of particular solutes at dislocations, which can influence their microstructure by altering locally the chemical composition [41]. Based on this, we investigated qualitatively the dislocation density in the different conditions and evaluated the segregation of solutes at dislocations, that can potentially enhance or facilitate the observed compositional alterations.

In particular, in the initial PX microstructure, there is almost no dislocation visible on ECCI images (Fig. 11a). Nevertheless, few linear dislocations segments can be seen by TEM, especially around γ'(I) precipitates (Fig. 11b), which have potentially originated from previous forging and cooling steps. This observation is in good agreement with a previous study where the same alloy in sub-solvus solution treated and aged state was investigated [40].

After holding at 760°C for 40 h, still no dislocations can be seen on ECCI images (Fig. 12a). By contrast, a noticeable density of dislocations (Fig. 12b) is present in the grains of the sample submitted
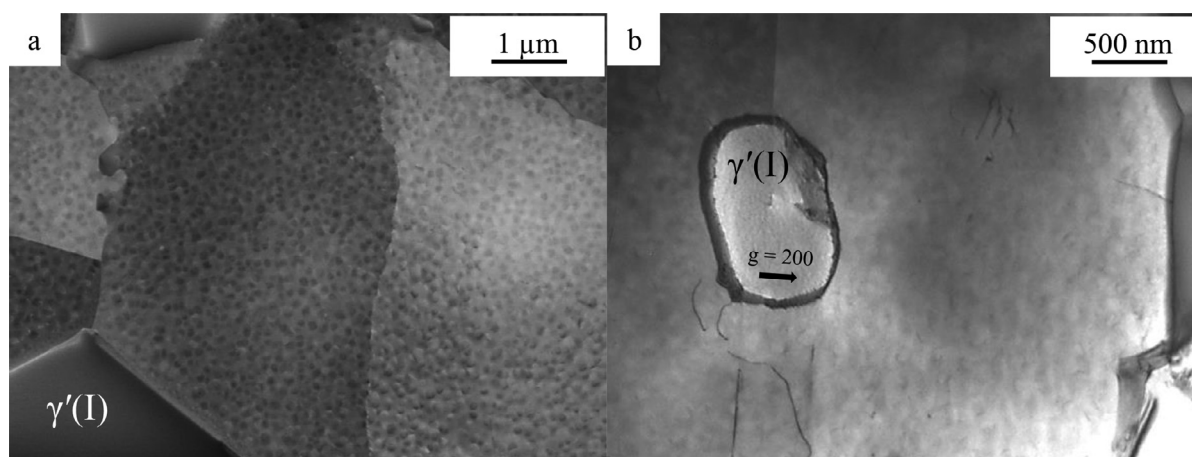
Table 6
Vegard coefficient values in the γ and γ' phases

	Elements	Co	Cr	Fe	Al	Ti	Mo	Nb
γ	Γ_i (Å/at.%)	0.0196	0.11	0.115	0.179	0.422	0.478	0.7
	Source	[39]	[39]	[11]	[39]	[39]	[39]	[39]
γ'	Γ_i (Å/at.%)	-0.014	-0.004	-0.004	/	0.258	0.208	0.46
	Source	[11]	[39]	[11]	/	[39]	[39]	[39]

Table 7
Lattice parameters of γ and γ' phases (obtained by Végard's law, Eq. (6), with the coefficients given in Table 6 and chemical compositions measured by APT) and deformation values associated with changes in composition during heat treatment or relaxation tests under 500 MPa at 760°C for 40 h.

		γ	γ'(II)	$a_{Vg}^{\gamma/\gamma'} = a_{Vg}^{\gamma} \cdot f_s^{\gamma} + a_{Vg}^{\gamma'} \cdot f_s^{\gamma'}$	ε_{APT}
PX Initial state	a_{Vg}(Å)	3.5856	3.6045	3.5918	/
	f_s (%)	67	33		
PX + 760°C /40 h	a_{Vg}(Å)	3.5828	3.6029	3.5912	- 0.017%
	f_s (%)	58	42		

Fig. 11. Initial state of the PX material observed by (a) ECCI and (b) TEM bright field imaging.

to relaxation testing from an initial stress of 500 MPa ($\varepsilon = 0.28\%$) at the same temperature. Dislocation density is even higher in primary precipitates (Fig. 12c), near grain boundaries and near primary precipitates (Fig. 12d).

The higher dislocation density in the case of the relaxation gauge sample after 500 MPa / 40 h at 760°C, allowed us to investigate a potential segregation of solutes at dislocations. Fig. 13 shows an APT reconstruction containing a γ/γ' interface from this alloy. Within the γ'(II) precipitate, a local enrichment of Cr is observed, along tubular features which reveals segregation onto dislocations (as often encountered by APT [42,43]). Note here that the observed local enrichment is associated with segregation to a dislocation, but not the dislocation itself, given the fact that dislocations cannot be directly observed by APT. 1D composition profiles across a dislocation in γ' (arrow #1 in Fig. 13a) are shown in Fig. 13b and c. A distinct segregation of Cr, Co and Fe at the dislocation is clearly visible (Fig. 13b). By contrast, depletion of Ni, Al and Ti is observed (Fig. 13c). Segregation of the same elements onto dislocations has been shown in other nickel-based superalloys after plastic deformation at high temperature [44–49]. In addition, Fig. 13d shows 1D composition profiles from the γ matrix along the dislocation as denoted by arrow #2 in Fig. 13a. Diffusion of Cr along the dislocation is apparent, while it is less pronounced in the case of Co and Fe. This is most likely related to the higher partitioning of Cr at the dislocation compared to Co and Fe.

In order to investigate any chemical alteration due to the segregation of solutes at dislocations in γ', the γ matrix composition close to the sheared $\gamma'$ precipitate in Fig. 13a is compared with the γ matrix composition next to γ' precipitates which are not sheared (Fig. 3c). The comparison between the solutes is given in Table 8. It is shown that a small depletion of Cr is observed in the γ matrix close to the sheared γ' precipitate, while Co and Fe are not influenced. The segregation of Cr is more pronounced compared to that of Co and Fe, which could potentially explain that no chemical alteration is observed for Co and Fe. By contrast, a slight increase of Ni is observed.

4. Discussion

It has been shown in the section n°3 (Results) that the unusual relaxation behavior of AD730™ at 760°C results from subtle microstructural evolutions, overall leading to the contraction of the specimen in the absence of any applied load. Such a contraction may have consequences in terms of dimensional changes of forged components that need to be taken into account during further manufacturing steps, more specifically for large dimension parts. In this discussion section, the γ/γ' lattice misfit evolution and the impact of chemical evolution evolutions at the phase scales with and without plastic activity will be discussed.

4.1. Lattice misfit of the AD730 alloy and its dependence on temperature

Some commercial polycrystalline superalloys have a slightly negative lattice misfit at room temperature such as Udimet™ 720Li [15] while others exhibit a slightly positive misfit at room
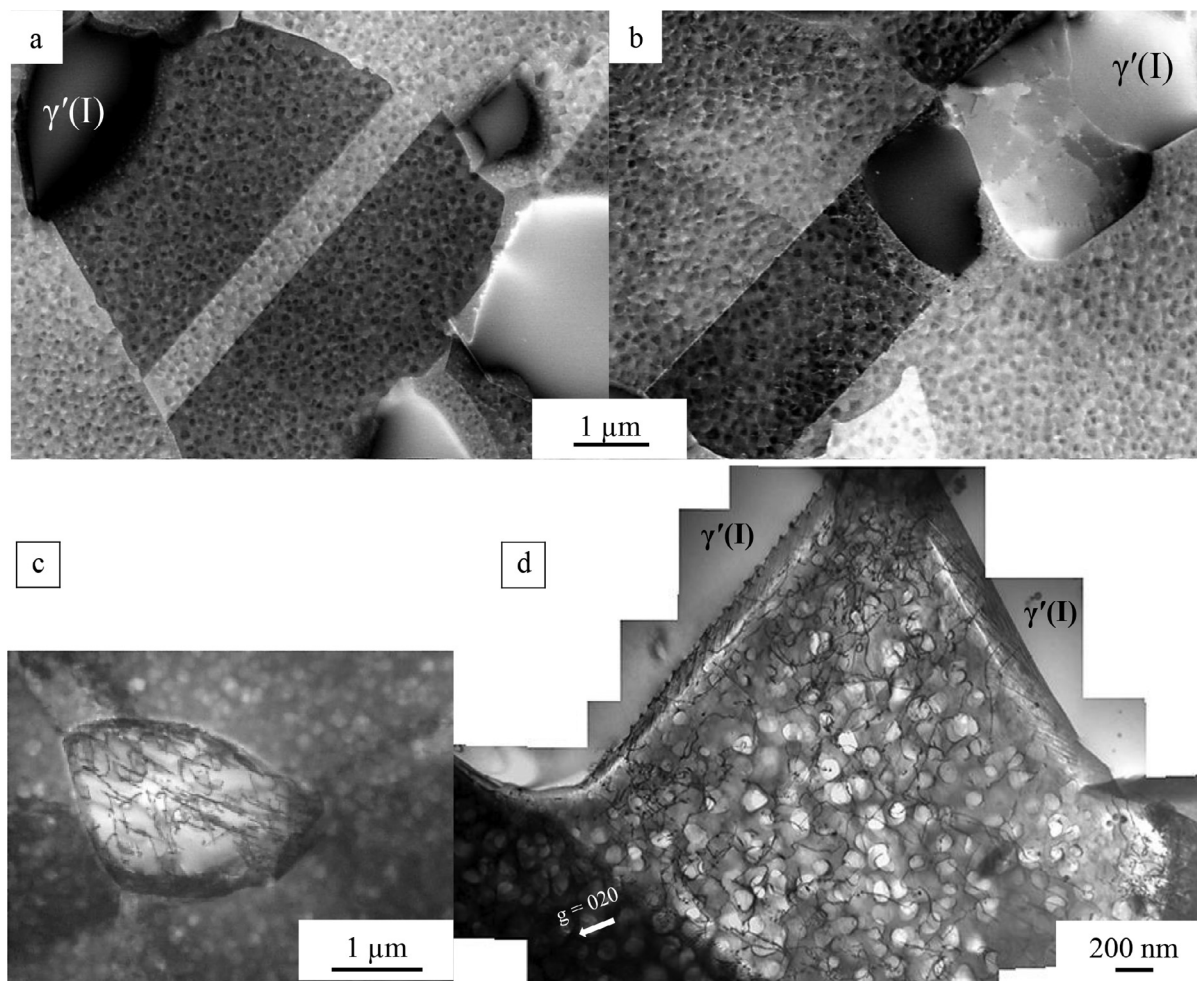
Fig. 12. (a) ECCI micrograph of the PX microstructure after 40 h holding at 760°C. (b) ECCI and (c,d) TEM bright field images of a PX sample after 40 h stress relaxation testing from 500 MPa initial stress at 760°C.

Table 8
Comparison of the composition between the γ matrix close to a γ' precipitate with a dislocation (Fig. 13a) and the γ matrix next to γ' precipitates which are not sheared (Fig. 3c) in the gauge sample after 500 MPa / 40 h at 760°C (at.%).

(at.%)	Gauge sample (no dislocations)	Gauge sample (with dislocations)	With dislocations – No dislocations
Cr	26.6 ± 0.8	25.4 ± 0.2	- 1.2
Co	12.1 ± 0.3	11.9 ± 0.1	- 0.2
Fe	5.9 ± 0.2	5.9 ± 0.3	0
Ni	45.8 ± 0.7	46.9 ± 0.3	+ 1.1
Al	2.0 ± 0.1	2.3 ± 0.2	+ 0.3
Ti	1.6 ± 0.1	1.7 ± 0.1	+ 0.1

temperature such as Waspaloy, Alloy 718 [50] or Rene 88 DT [20]. Other high γ' phase volume fraction (blade) superalloys such as CMSX-4 [51,52], TMS12 [2], IN738LC [53] or SC16 [34] behave similarly to AD730™ superalloy with a positive misfit at room temperature that becomes negative at higher temperatures. Fig. 5 shows that the lattice misfit as deduced from XRD data is slightly positive at room temperature and tends toward 0 while approaching 760°C as the contribution of the γ and γ' phases can no longer be discerned at this temperature. The γ'(II) precipitates in this alloy have been reported to coalesce perpendicular to the tensile load during creep at 850°C and 900°C of single crystalline specimens (Fig. III-18-c in the Ref. [22] and Fig. 7d in the Ref. [54]), which proves that the misfit is negative in this high temperature range.

If the lattice misfit tends towards 0 at 760°C as suggested by the XRD results on SX specimens, the morphology of the γ'(II) precipitates should tend to adopt spherical shape after prolonged holding time at 760°C [28,53,55]. This is true as shown on Fig. 14 compares the γ'(II) morphology in the PX initial state and after long-term holding (312 h) at 760°C.

The lattice misfit of AD730™ alloy is close to zero at 760°C. During holding at 760°C, it should be noted that the FWHM of the (400) diffraction peak increases during the first 20 h (Fig. 15), suggesting that the lattice parameters of the two phases are close but evolves in a different way.

4.2. The mechanism for isothermal macroscopic contraction

As revealed by APT, the chemical composition of both the γ matrix and the γ'(II) and γ'(III) precipitates of the PX microstructure varied during holding at 760°C. A redistribution of chemical elements between the matrix and these same precipitates is ob-
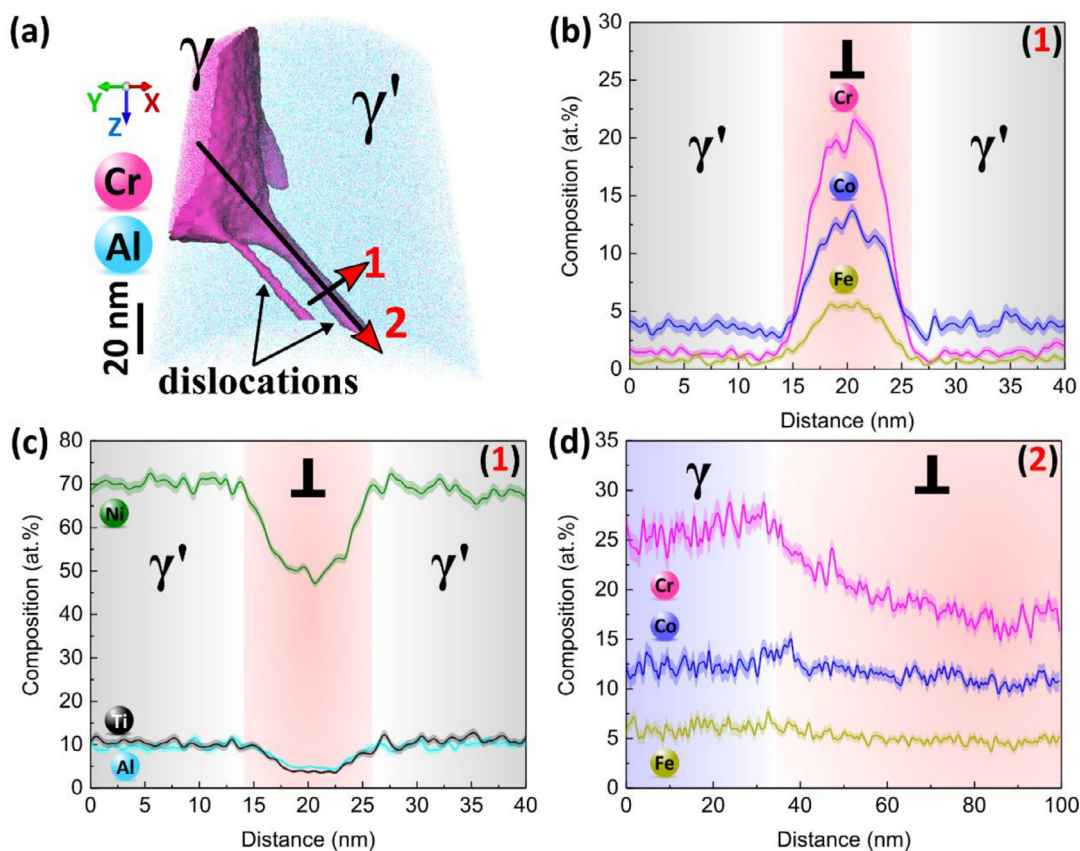
Fig. 13. (a) Atom probe reconstruction from AD730^{TM} region showing a γ/γ' interface and dislocations in γ' phase. γ/γ' interface and dislocations are shown with an iso-composition surface at 13 at.% Cr. (b) Cr, Co and Fe 1D concentration profiles and (c) Ni, Al, Ti 1D concentration profiles across the dislocation #1. (d) Cr, Co and Fe 1D concentration profiles along the dislocation #2.
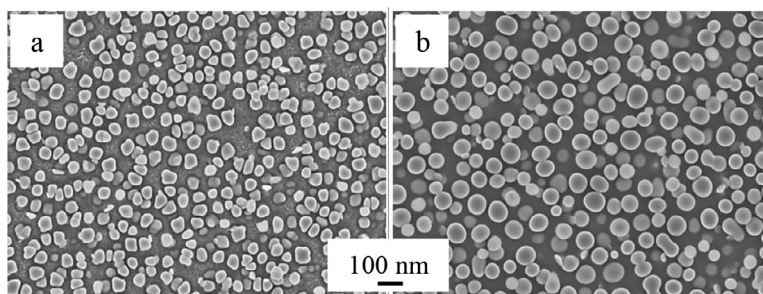
Fig. 14. γ'(II) spheroidization during heat treatment at 760°C. γ'(II) precipitates (a) in the PX originated from a γ'-subsolvus solutioning heat treatment at 1080°C followed by cooling at 100°C/min initial state and (b) after 312 h holding at 760°C followed by water quench.

served over a significant number of elements (Ni, Al, Cr, Ti and Co - Fig. 4). With the heat treatment at 760°C, γ' precipitates reject Cr and Co and consume Ni, Al and Ti (γ' formers) to reach equilibrium.

Applying the Vegard's law with coefficient values found in literature and the acquired APT data from the PX samples (see Section 3.1.3) showed that both the lattice parameters of the γ matrix and that of the γ'(II) precipitates decrease. A simple linear rule of mixture considering the area fractions and the lattice parameters of the matrix and of the γ'(II) precipitates leads to an overall contraction of about 0.020%, a value very close to the macroscopic contraction measured by isothermal dilatometry over the same period of time (~25h) (Fig. 1). This may sound surprising since primary and tertiary precipitates are omitted in the calculation, but can be explained by the fact that the secondary precipitates account for the largest area fraction (33%) compared to γ'(I)

precipitates (5%) and γ'(III) precipitates (low fraction which could not be measured).

In order to better assess the reason why both the lattice parameters happen to decrease as a result of elemental redistribution between the matrix and precipitates, the lattice parameter variation associated with the chemical composition variation has been calculated thanks to the Vegard law coefficients, for each element and each phase. The results are listed in Table 9 and plotted on Fig. 16.

This brings out the role of each element in each phase and suggests that the decrease of the parameter is mainly driven:

- by Al, Ti, Nb not fully compensate by the effect of Cr in the γ matrix
- by Ti and Nb not fully compensate by the effect of Co in the γ' precipitates

Table 9

Chemical composition and composition difference (atomic %) of secondary precipitates and matrix before and after heat treatment at 760°C for 40 h.

		Ni	Al	Cr	Ti	Mo	Nb	Co	Fe
γ	PX initial state (%at)	47.2	2,9	23.8	2.2	2.2	0.3	11.2	5.3
	PX + 760°C / 40 h (%at)	45.4	2	26	1.5	2.2	0.1	12.4	5.8
	Δi (%at)	-1.8	-0.9	2.2	-0.7	0	-0.2	1.2	0.5
	Δi × Γi (Å)	/	-0.161	0,242	-0.295	0	-0.140	0.024	0.058
γ'(II)	PX initial state (%at)	65.9	10	1.5	11.0	0.4	1.3	4.4	0.8
	PX + 760°C / 40 h (%at)	69.8	10.5	1.1	10.8	0.4	1.0	2.7	0.6
	Δi (%at)	3.9	0.5	-0.4	-0.2	0	-0.3	-1.7	-0.2
	Δi × Γi (Å)	/	/	0.002	-0.052	0	-0.138	0.024	0.001
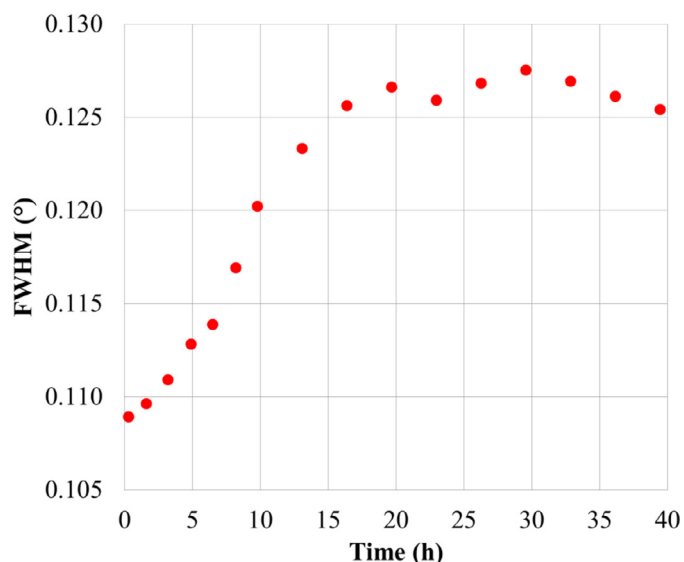
Fig. 15. FWHM (Full Width at Half Maximum) of the (400) γ/γ' Cu-Kα₁ diffraction peak during isothermal heat treatment at 760°C of SX specimen, as a function of holding time.

The Vegard's analysis plotted this way emphasizes that the effect of each element on the lattice parameters is not a simple steric issue with volume conservation of atoms seen as hard spheres, and that chemical redistributions between two phases can indeed lead to the decrease of both the parameters.

In the SX version of the alloy, a decrease of the lattice parameter by 0.042% was measured by XRD after 40 h (Fig. 6) at 760°C. This decrease mainly occurs during the first 25–30 h, again

the same time as that typical one observed for the PX material (Fig. 10). Because the changes in lattice parameter occurring at 760°C are related to irreversible local chemical changes, the XRD peak profiles at room temperature are different before and after the *in-situ* annealing heat treatment (40 h at 760°C). From the γ and γ' peaks positions on the diffractogram (Figs. 7–9), the change in the room temperature lattice parameter of the γ matrix before and after 40 h holding at 760°C was estimated to be greater than that of the γ' precipitates, 0.053% and 0.028%, respectively. Combining these values and the precipitate area fraction (43%) leads to an overall decrease by 0.042%, consistent with isothermal dilatometry test.

The macroscopic contraction measured by isothermal dilatometry compares very well with the relative changes in lattice parameter assessed *in-situ* by XRD (Fig. 10), for both the SX and the PX alloys. This strongly suggests that the isothermal volume contraction is mainly controlled by the changes in the lattice parameters of the γ' precipitates and γ matrix, which themselves result from local scale atomic diffusion and chemical equilibration. The compositional changes in the matrix and precipitates cause a decrease in the lattice parameter and thus explain both the macroscopic contraction and the relaxation retardation observed over the first 25 h at 760°C (Fig. 1). These results are also in good agreement with a recent study on the stress relaxation behavior of powder metallurgy superalloys where the initial applied strain was 0.6% [56] or with our preliminary work showing no abnormal relaxation behavior once γ'(III) precipitates have been dissolved at 760°C by a prior long-term pre-aging [5].

Contraction was also observed in other nickel-based superalloys during heat treatment such as Waspaloy [11], RR1000 [10], Inconel 718 [7], Inconel 783 [8] or IN100 [9], with a magnitude which is similar to what was observed in the present work (Table 10).

a)   γ matrix

b) γ'(II) precipitates
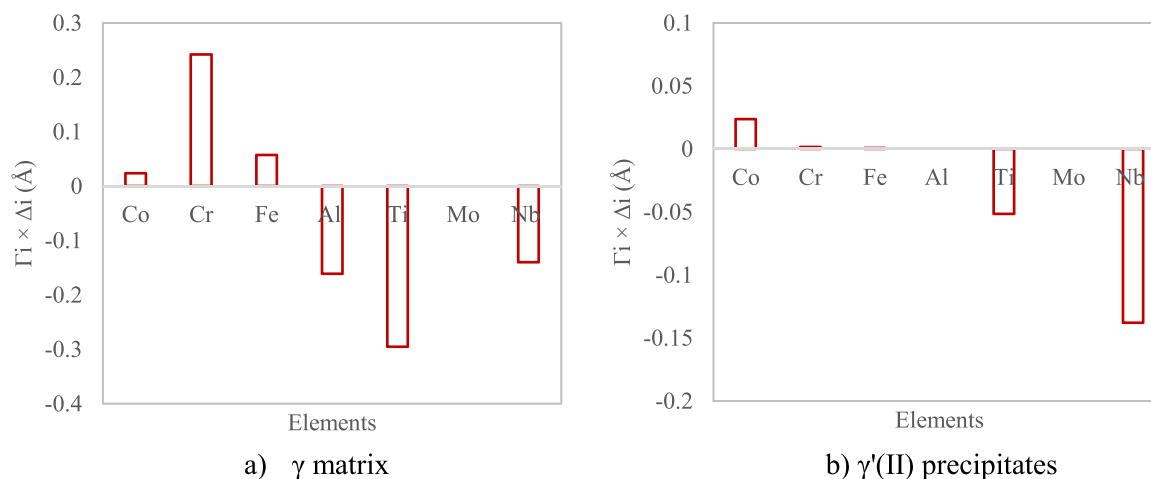
Fig. 16. Variation in lattice parameter (Γi × Δi) associated with the chemical composition variation for each element and each phase calculated from Vegard's law.

Table 10

Comparison of macroscopic contraction measured by dilatometry (in black), XRD (in red) and Vegard's law (in green) for different super-alloys at different temperatures for a time after stabilization.

Contraction (%)	AD730™[This work]	Waspaloy [11]	RR1000 [10]	Inconel 718 [7]	Inconel 783 [8]	IN100 [9]
PX	**0.016** (760°C) **0.017** (760 ○ C) **0.017** (760 ○ C) *25* h	**0.032** (550°C) *10000* h	**0.055** (760 ○ C) *16* h	**0.020** (500°C) *8 h* **0.060** (620°C) *8 h* **0.080** (720°C) *8 h*	**0.027** (482°C) *500* h **0.035** (538°C) *300* h **0.017** (593°C) *100* h	**0.095** (704°C) *300* h
SX	**0.042** (760 ○ C) *25* h					
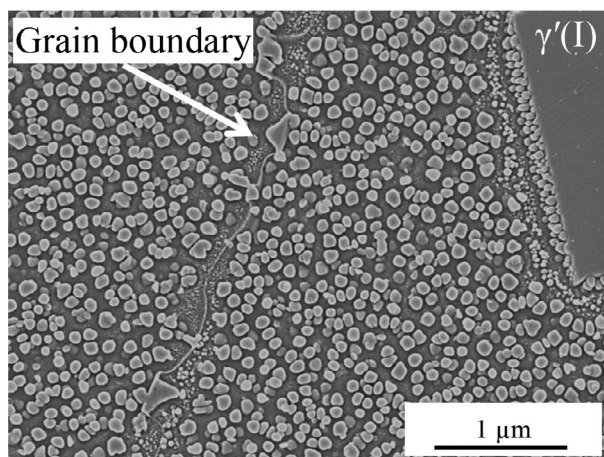
Fig. 17. γ' phase topology near to and further away from a grain boundary. SEM/SE micrograph.

Note worthily, in the present work, the ultimate measured contraction was about 0.042% in the SX alloy, while it was only 0.017% in the PX alloy (XRD measurements - Fig. 10). There are several possible explanations for the difference between PX and SX contraction magnitude. The first obvious one is anisotropy since the SX material is tested and observed along a nearly <001> crystallographic direction, whereas the forged PX materials are known to have no or very weak crystallographic texture. Then, the volume fraction of γ'(II) precipitates is greater in the SX microstructure compared to the PX. The SX microstructure has indeed been tailored by preliminary thermal treatments to be close to the intragranular microstructure of the polycrystalline version of the alloy (Fig. 2 and related text in Section 2.1). The size of the secondary precipitates is similar but their area fraction (43%), and thus their number per unit area/volume, is higher in the SX compared to the PX material (33%) due to primary precipitates (accounting for 5% area in the PX and zero in the SX material) and tertiary precipitates. The matrix channels between the γ'(II) precipitates are thus narrower in the SX which could affect both the diffusion profiles and the actual average value of the matrix lattice parameter (accounting for the constrained value near to the interface and that further away). Another difference to be considered is the presence of grain boundaries in the polycrystalline version of the alloy, which might lead to specific local mechanisms and contraction magnitude notably as a result of differences in precipitate topology compared to the grain interior (Fig. 17). Indeed, a 150 nm wide zone depleted in precipitate γ'(II) is observed on both sides of the grain boundary and coarser γ'(II) are located on the grain boundaries. Further work is needed to describe the local mechanisms at play at grain boundaries and their role in the macroscopic behavior.

4.3. Potential local chemical alterations by pipe diffusion of solutes along dislocations

When a dislocation shears a γ'(II) precipitate, it can stay trapped within it. In this case, APT has shown that Cr, Co and Fe elements have been found to preferentially partition along dislocations (Fig. 13). The proposed scenario can be understood as a consequence of the mass transport via pipe diffusion along these dislocations [57]. The diffusion of Cr, Co and Fe from the matrix to the γ'(II) precipitate can then lead to a local depletion of those elements in the matrix. Other elements such as Ni, Al and Ti will thus consequently have higher amounts in γ matrix. Indications of such chemical alteration are shown in Table 8, where the γ matrix close to a shared with dislocation γ' precipitate (Fig. 13a) is compared with the γ matrix next to γ' precipitates which are not sheared (Fig. 3c) in the same sample. In particular, the presence of dislocations in the γ' precipitates could be possibly associated with the lower amounts of Cr in the surrounding γ matrix. Thus, a plausible scenario could involve a correlation between the dislocation density in the γ' precipitates and the depletion of Cr from the matrix. Potentially, the higher the dislocation density within the γ' precipitates, the greater the local chemical inhomogeneities, however this needs to be further investigated with a different set of experimental plan. Similar effect on chemical alterations as a result of the presence of dislocations is reported in a polycrystalline superalloy after local deformation by oxidized carbide [58]. Given the presence of dislocations and the related chemical segregation at them, a chemical evolution of the matrix is observed that is different from the sample without dislocations. Thus, dislocations could potentially promote chemical evolutions that, in turn, may also influence the lattice parameter of the macroscopic contraction. However, the actual relative contribution of plasticity on the macroscopic contraction through its impact of chemical element distribution remains to be objectively measured.

5. Conclusion

In this work the mechanisms controlling the macroscopic contraction in the AD730™ alloy at a typical stress relaxation temperature (760°C) was studied. Analyses from macro to nano scales (XRD, ECCI, TEM and APT) were performed on as-received, heat treated and stress-relaxed specimens. The studied phenomenon is of significant practical importance since the intrinsic tendency for isothermal contraction retards stress relaxation, could also affect the creep behavior of the alloy and lead to non-negligible dimensional changes of large components. This work shows that changes in chemical composition at a very fine scale (that of secondary precipitates) actually control this macroscopic behavior. More precisely, the following conclusions can be drawn:

- During isothermal holding at 760°C, Ni, Al and Ti contents decrease in the matrix and increase in the γ'(II) precipitates while Cr, Co and Fe contents increase in the matrix and decrease in

the γ' precipitates. These compositional changes induce a lattice parameter decrease of both γ and γ' phases, which spans over during the first 25 h. This decrease in the lattice parameter is of comparable magnitude with the macroscopic contraction measured by isothermal dilatometry (-0.017% for the polycrystalline alloy and -0.042% for the monogranular variant, after 25 h).

- Partitioning of Cr, Co and Fe at dislocations within γ'(II) caused by deformation was revealed by APT. This partitioning causes local chemical inhomogeneities in the γ matrix which results from the mass transport via pipe diffusion along these dislocations of Cr and to a lower extent of the concentration Co. As a result of these elements in the matrix is lower in the presence of dislocation compared to the matrix without dislocations. This way the presence of dislocations is likely to affect the chemical redistribution kinetics and possibly amplitude.

- Moreover, careful XRD analyses along with *in-situ* annealing showed that the misfit of the AD730$^{\text{TM}}$ alloy is low and positive at room temperature and tends towards a zero value at 760°C, consistent with the progressive spheroidization of the secondary precipitate morphology at this temperature.

Declaration of Competing Interest

The authors declare that they have no known competing financial interests or personal relationships that could have appeared to influence the work reported in this paper.

CRediT authorship contribution statement

Malik Durand: Investigation, Formal analysis, Visualization, Writing – original draft, Writing – review & editing. **Jonathan Cormier:** Investigation, Supervision, Conceptualization, Resources, Writing – review & editing. **Fabien Paumier:** Investigation, Formal analysis. **Shyam Katnagallu:** Investigation. **Aparna Saksena:** Investigation, Formal analysis. **Paraskevas Kontis:** Investigation, Formal analysis, Writing – review & editing. **Florence Pettinari-Sturmel:** Investigation, Formal analysis. **Muriel Hantcherli:** Investigation, Formal analysis. **Jean-Michel Franchet:** Supervision, Resources, Conceptualization, Funding acquisition. **Christian Dumont:** Investigation, Resources. **Nathalie Bozzolo:** Writing – review & editing, Supervision, Conceptualization, Funding acquisition, Project administration.

Acknowledgments

References

[1] T.M. Pollock, S. Tin, Nickel-based superalloys for advanced turbine engines: chemistry, microstructure and properties, J. Propuls. Power 22 (2006) 361–374.

[2] R. R.C, The Superalloys Fundamental and Applications, University Press, Cambridge, 2006.

[3] M.A. Rist, J.A. James, S. Tin, B.A. Roder, M. Daymond, Residual stresses in a quenched superalloy turbine disc: measurements and modeling, Metall. Mater. Trans. A 37 (2006) 459–467.

[4] M. Karadge, B. Grant, P.J. Withers, G.J. Baxter, M. Preuss, Thermal relaxation of residual stresses in Nickel-based superalloy inertia friction welds, Metall. Mater. Trans. A 42 (2011) 2301–2311.

[5] M. Durand, J. Cormier, P. Villechaise, J-M. Franchet, C. Dumont, N. Bozzolo, Metallurgical mechanisms upon stress relaxation annealing of the AD730TM superalloy, in: Proceedings of the Paper Presented Superalloys, 2020, pp. 546–557.

[6] M. Nazmy, C. Gerdes, The relaxation behavior of high Chromium-Ni base superalloys, in: Proceedings of the Paper presented at Euro Superalloys, 2010, pp. 321–326.

[7] H. Qin, Z. Bi, D. Li, R.Y. Zhang, T.L. Lee, G. Feng, H.B. Dong, J. Du, J. Zhang, Study of precipitation-assisted stress relaxation and creep behavior during the ageing of a nickel iron superalloy, Mater. Sci. Eng. A 742 (2019) 493–500.

[8] M.G. Fahrmann, A.A. Wereszczak, T.P. Kirkland, Stress relaxation behavior and dimensional stability of INCONEL® alloy 783, Mater. Sci. Eng. A 271 (1999) 122–127.

[9] S.K. Sondhi, B.F. Dyson, M. McLean, Tension–compression creep asymmetry in a turbine disc superalloy: roles of internal stress and thermal ageing, Acta Mater. 52 (2004) 1761–1772.

[10] D.M. Collins, L. Yan, E.A. Marquis, L.D. Connor, J.J. Ciardiello, A.D. Evans, H.J. Stone, Lattice misfit during ageing of a polycrystalline nickel-base superalloy, Acta Mater. 61 (2013) 7791–7804.

[11] S. Kinzel, J. Gabel, R. Völkl, U. Glatzel, Reasons for volume contraction after long term annealing of Waspaloy, Adv. Eng. Mater. 17 (2015) 1106–1112.

[12] J. Cormier, P. Gadaud, M. Czaplicki, R.Y. Zhang, H.B. Dong, T.M. Smith, F. Zhang, J.S. Tiley, S.L. Semiatin, *In-situ* determination of precipitation kinetics during heat treatment of superalloy 718, Metall. Mater. Trans. A 52 (2020) 500–511.

[13] A. Devaux, E. Georges, P. Héritier, Properties of new C&W superalloys for high temperature disk applications, in: Proceedings of the Paper presented at Superalloy 718 and Derivatives, 2010, pp. 223–235.

[14] A. Devaux, E. Georges, P. Héritier, Development of new C&W superalloys for high temperature disk applications, in: Proceedings of the Paper presented at Euro Superalloys, 2010, pp. 405–410.

[15] M.P. Jackson, R.C. Reed, Heat treatment of Udimet 720Li: the effect of microstructure on properties, Mater. Sci. Eng. A 259 (1999) 85–97.

[16] R. Radis, M. Schaffer, M. Albu, K. Gerald, Evolution of size and morphology of γ' precipitates in Udimet 720 Li during continuous cooling, in: Proceedings of the Paper presented at Superalloys, 2008, pp. 829–836.

[17] F. Masoumi, D. Shahriari, M. Jahazi, J. Cormier, A. Devaux, Kinetics and mechanisms of γ' reprecipitation in a Ni-based superalloy, Sci. Rep. 6 (2016) 28650 Art.

[18] A. Devaux, A. Helstroffer, J. Cormier, P. Villechaise, J. Douin, M. Hantcherli, F. Pettinari-Sturmel, Effect of aging heat-treatment on mechanical properties of AD730TM superalloy, in: Proceedings of the Paper presented at Superalloy 718 and Derivatives, 2014, pp. 521–535.

[19] F. Masoumi, M. Jahazi, D. Shahriari, J. Cormier, Coarsening and dissolution of γ' precipitates during solution treatment of AD730TM Ni-based superalloy: mechanisms and kinetics models, J. Alloy. Compd. 658 (2016) 981–995.

[20] S.T. Wlodek, M. Kelly, D.A. Alden, The structure of Rene 88 DT, in: Proceedings of the Paper presented at Superalloys, 1996, pp. 467–476.

[21] R.J. Mitchell, M. Preuss, M.C. Hardy, S. Tin, Influence of composition and cooling rate on constrained and unconstrained lattice parameters in advanced polycrystalline nickel base superalloys, Mat. Sci. Eng. A 423 (2006) 282–291.

[22] L. Thébaud, Etude Des Relations 785 Entre Microstructure et Propriétés Mécaniques du Nouveau Superalliage Base Nickel AD730TM, École Nationale Supérieure de Mécanique et d'Aérotechnique, Poitiers, 2017 [ed.] Ph.D Thesis. https://tel.archives-ouvertes.fr/tel-01735104/document.

[23] S. Vernier, Évolution de la Microstructure du Superalliage Base Nickel AD730 au Cours des Opérations de Forgeage Industrielles, Ecole Nationale des Mines de Paris - CEMEF, Sophia Antipolis, 2018 [ed.] Ph.D Thesis. https://pastel.archives-ouvertes.fr/tel-02149391/document.

[24] K. Thompson, D. Lawrence, D.J. Larson, J.D. Olson, T.F. Kelly, B. Gorman, *In situ* site-specific specimen preparation for atom probe tomography, Ultramicroscopy 107 (2007) 131–139.

[25] B. Gault, A.J. Breen, Y. Chang, J. He, Interfaces and defect composition at the near atomic scale through atom probe tomography investigations, J. Mater. Res. 33 (2018) 4018–4030.

[26] B. Lacroix, in: Influence des Défauts Cristallins sur les Changements de Phase Induits par Faisceaux d'ions Dans les Films Minces d'oxyde d'yttrium Y_2O_3, Université de Poitiers, Poitiers, 2009, p. Chapter 4. [ed.] Ph.D. Thesis.s.n.

[27] D.M. Collins, N. D'Souza, C. Panwisawas, C. Papadaki, G.D. West, A. Kostka, P. Kontis, Spinodal decomposition versus classical γ' nucleation in a nickel-base superalloy powder: An *in-situ* neutron diffraction and atomic-scale analysis, Acta Mater. 200 (2020) 959–970.

[28] R.A. Ricks, The growth of γ' precipitates in nickel-base superalloys, Acta Metall. 31 (1983) 43–53.

[29] D. Siebörger, H. Brehm, F. Wunderlich, D. Möller, U. Glatzel, Temperature dependence of lattice parameter, misfit and thermal expansion coefficient of matrix, γ' phase and superalloy, Z. Metallkunde 92 (2001) 58–61.

[30] A. Royer, P. Bastie, D. Bellet, J.L. Strudel, Temperature dependence of the lattice mismatch of the AM1 superalloy influence of the γ' precipitates morphology, Philos. Mag. A 72 (1995) 669–689.

[31] A. Royer, P. Bastie, M. Veron, *In situ* determination of γ' phase volume fraction and of relations between lattice parameters and precipitate morphology in Ni-based single crystal superalloy, Acta Mater. 46 (1998) 5357–5368.

[32] M.V. Nathal, R.A. Mackay, R.G. Garlick, Temperature dependence of γ-γ' lattice mismatch in nickel-base superalloys, Mater. Sci. Eng. 75 (1985) 195–205.

[33] W. Chen, N. Daroski, I. Zizak, G. Schumacher, H. Klingelhöffer, W. Neumann, Lattice distortion in γ' precipitates of single crystal superalloy SC16 under creep deformation, Nucl. Instrum. Methods Phys. Res. Sect. B 246 (2006) 201–205.

[34] G. Bruno, G. Schumacher, H. Cavalcanti Pinto, C. Schulze, Measurement of the lattice misfit of the nickel-base superalloy SC16 by high-energy synchrotron radiation, Metall. Mater. Trans. A 34 (2003) 193–197.

[35] H. Biermann, M. Strehler, H. Mughrabi, High-temperature measurements of lattice parameters and internal stresses of a creep-deformed monocrystalline nickel-base superalloy, Metall. Mater. Trans. A 27 (1996) 1003–1014.

[36] M. Arnoux, Etude du Comportement en Fluage à Haute Température du Superalliage Monocristallin à Base de Nickel MCNG: Effet d'une Surchauffe, ISAE-ENSMA Ecole Nationale Supérieure de Mécanique et d'Aérotechnique – Poitiers, Poitiers, 2009 [ed.] Ph.D Thesiss https://tel.archives-ouvertes.fr/tel-00445811/document.

[37] G.C. Weatherly, R.B. Nicholson, An electron microscope investigation of the interfacial structure of semi-coherent precipitates, Philos. Mag. J. Theor. Exp. Appl. Phys. 17 (1968) 801–831.

[38] T.M. Pollock, A.S. Argon, Directional coarsening in nickel-base single crystals with high volume fractions of coherent precipitates, Acta Metall. Mater. 42 (1994) 1859–1874.

[39] P. Caron, High γ' solvus new generation nickel-based superalloys for single crystal turbine blade applications, in: Proceedings of the Paper presented at Superalloys, 2000, pp. 737–746.

[40] F. Pettinari-Sturmel, J. Douin, F. Krieg, E. Fleischmann, U. Glatzel, Evidence of short-range order (SRO) by dislocation analysis in single-crystal ni-based matrix alloys with varying re content after creep, in: Proceedings of the Paper presented at Superalloys, 2020, pp. 253–259.

[41] P. Kontis, Interactions of solutes with crystal defects: a new dynamic design parameter for advanced alloys, Scr. Mater. 194 (2021) 1–8.

[42] E.C D.Blavette, A. Fraczkiewicz, A. Menand, Three-dimensional atomic-scale imaging of impurity segregation to line defect, Science 286 (1999) 2317–2319.

[43] J. Wilde, A. Cerezo, G.D.W. Smith, Three-dimensional atomic-scale mapping of a cottrell atmosphere around a dislocation in iron, Scr. Mater. 43 (2000) 39–48.

[44] P. Kontis, Z. Li, D.M. Collins, J. Cormier, D. Raabe, B. Gault, The effects of chromium and cobalt segregation at dislocations on nickel-based superalloys, Scr. Mater. 145 (2018) 76–80.

[45] A. Cervellon, S. Hémery, P. Kürnsteiner, B. Gault, P. Kontis, J. Cormier, Crack initiation mechanisms during very high cycle fatigue of Ni-based single crystal superalloys at high temperature, Acta Mater. 188 (2020) 131–144.

[46] X. Wu, S.K. Makineni, P. Kontis, G. Dehm, D. Raabe, B. Gault, G. Eggeler, On the segregation of Re at dislocations in the γ' phase of Ni-based single crystal superalloys, Materialia 4 (2018) 104–114.

[47] S. Hamadi, F. Hamon, J. Delautre, J. Cormier, P. Villechaise, S. Utada, P. Kontis, N. Bozzolo, Consequences of a room-temperature plastic deformation during processing on creep durability of a Ni-based SX superalloy, Metall. Mater. Trans. A 49 (2018) 4246–4261.

[48] S. Katnagallu, S. Vernier, M-A. Charpagne, B. Gault, N. Bozzolo, P. Kontis, Nucleation mechanism of hetero-epitaxial recrystallization in wrought nickel-based superalloys, Scr. Mater. 191 (2021) 7–11.

[49] L. Thebaud, P. Villechaise, C. Crozet, A. Devaux, D. Bechet, J-M. Franchet, A-L. Rouffié, M. Mills, J. Cormier, Is there an optimal grain size for creep resistance in Ni-based disk superalloys? Mater. Sci. Eng. A 716 (2018) 274–283.

[50] J. Coakley, D. Ma, M. Frost, D. Dye, D.N. Seidman, D.C. Dunand, H.J. Stone, Lattice strain evolution and load partitioning during creep of a Ni-based superalloy single crystal with rafted γ' microstructure, Acta Mater. 135 (2017) 77–87.

[51] T. Yokokawa, K. Ohno, H. Murakami, T. Kobayashi, T. Yamagata, H. Harada, Accurate measurement of lattice misfit between γ and γ' phases in nickel-base superalloys at high temperatures, Adv. X Ray Anal. 39 (1995) 449–456.

[52] P. Strunz, M. Petrenec, V. Davydov, J. Polak, P. Beran, Misfit in Inconel-type superalloy, Adv. Mater. Sci. Eng. 2013 (2013) 1–7.

[53] Y.S. Yoo, D.Y. Yoon, M.F. Henry, The effect of elastic misfit strain on the morphological evolution of γ'-precipitates in a model Ni-base superalloy, Met. Mater. 1 (1995) 47–61.

[54] W-D. Cao, R. Kennedy, Role of chemistry in 718-type alloys: Allvac 718plus alloys development, in: Proceedings of the Paper Presented at Superalloys, 2004, pp. 91–99.

[55] N. Mrozowski, G. Hénaff, F. Hamon, A-L. Rouffié, J-M. Franchet, J. Cormier, P. Villechaise, Aging of γ' precipitates at 750 °C in the nickel-based superalloy AD730TM: a thermally or thermos-mechanically controlled process? Metals 10 (2020) 426 1 -19.

[56] L. Li, E. Sun, S. Tin, Microstructure dependance of stress relaxation behavior of powder-processed Ni-base superalloys, Mater. Sci. Eng. A 814 (2021) 141146.

[57] M. Legros, G. Dehm, E. Arzt, T.J. Balk, Observation of giant diffusivity along dislocation cores, Science 319 (2008) 1646 1649.

[58] P. Kontis, Z. Li, M. Segersäll, J.J. Moverare, R.C. Reed, D. Raabe, B. Gault, The role of oxidized carbides on thermal-mechanical performance of polycrystalline superalloys, Metall. Mater. Trans. A 49 (2018) 4236-4235.